Case Studies in Construction Materials 20 (2024) e03032

Contents lists available at ScienceDirect

Case Studies in Construction Materials

journal homepage: www.elsevier.com/locate/cscm

Finite element method for sustainable and resilient structures made with bar and fiber -reinforced EAFS concrete

Aratz Garcia-Llona [a,*], Ignacio Piñero [b,c], Vanesa Ortega-López [d], Amaia Santamaría [e], Miquel Aguirre [f,g]

[a] Mines Saint-Etienne, Univ Lyon, Univ Jean Monnet, Etablissement Français du Sang, INSERM, U 1059 Sainbiose, Saint-Etienne F-42023, France
[b] Tecnalia, Basque Research and Technology Alliance (BRTA), Astondo Bidea, Edificio 700, Derio 48160, Spain
[c] Universidad Europea de Valencia. School of Architecture & Polytechnic. Department of Architecture, Engineering and Design (STEAM), Paseo de la Alameda, 7, Valencia 46010, Spain
[d] Department of Civil Engineering, University of Burgos, Escuela Politécnica Superior, Calle Villadiego s/n, Burgos 09001, Spain
[e] Department of Mechanical Engineering, University of the Basque Country (UPV/EHU), Escuela de Ingeniería de Bilbao, Plaza Ingeniero Torres Quevedo, 1, Bilbao 48013, Spain
[f] Laboratori de Càlcul Numèric, Universitat Politècnica de Catalunya, Jordi Girona 1, Barcelona E-08034, Spain
[g] International Centre for Numerical Methods in Engineering (CIMNE), Gran Capità, Barcelona 08034, Spain

ARTICLE INFO

Keywords:
Fracture mechanics
Reinforced concrete
Electric Arc Furnace Slag
Fiber reinforced
Interface solid finite elements

ABSTRACT

Structural engineers have to address the climate change challenge by designing sustainable and resilient structures. At this juncture, Electric Arc Furnace Slags (EAFS), a steel-industry waste, are used in replacement of natural aggregates to enhance concrete properties. Moreover, steel and synthetic fibers are added to improve the postcracking behavior while the traditional bar reinforcement enhances the tensile performance. This makes EAFS concrete substantially ductile compared to normal concrete, which contributes to a higher structural resiliency, and hence minimizes functionality disruptions. However the use of fiber and bar -reinforced EAFS concrete in structures is still limited due to the uncertainties introduced by EAFS and fibers. This justify the development of advanced modeling techniques (ie. Finite element Analysis, FEA), which can be used to predict the behavior of EAFS concrete structures at the designing stage. This work build up from the extensive work of the coauthors in the testing of EAFS concrete and, more recently, in the developed FEA of fiber-reinforced EAFS concrete. In this paper the modeling of bar reinforcement is added to the FEA to study the behavior of structural elements made with fiber-reinforced EAFS concrete. The presented FEA is validated through full-scale experiments (four-point flexural test), which shows that the presented FEA is appropriate. The presented numerical model enables to study phenomena difficult to study from experiments or in-situ such as the cracking. It is worth noting that the addition of steel fibers reduced the crack mouth opening displacement in 29.3% and the depth of the cracks in 12.7% in the presented EAFS concrete.

1. Introduction

In recent years, construction industry is seeking to environmentally sustainable and resilient concrete structures [1–5].

* Corresponding author.
E-mail address: aratz.garciallona@emse.fr (A. Garcia-Llona).

https://doi.org/10.1016/j.cscm.2024.e03032
Received 19 September 2023; Received in revised form 4 January 2024; Accepted 4 March 2024
Available online 5 March 2024

Sustainability refers to its ability to reside in harmony with its natural surroundings by limiting the negative environmental impact of building constructions and operations. Instead of extracting natural material, the reuse of materials can be a good contribution to achieve such objective. To this end there is an increasing interest in eco-friendly concrete where natural aggregates are replaced [6–11] or the amount of cement is reduced [12–15], among other measures. In this research work, Electric Arc Furnace Slags (EAFS), a waste of steel-producing industry, are used as substitute for natural aggregates to manufacture a concrete with good performance while the environmental impact is reduced.

EAFS concrete shows great mechanical performance and durability [7,16–20]. The porous nature of EAFS provides a strong interlocking effect between the aggregates and the cement paste [18,21,22]. This results into higher compression and shear strength than concretes made with natural aggregates [19,23]. EAFS aggregates also increase the impermeability of concrete [23,24] and, therefore, the durability of the material. Finally, it also responds better to incidences such as carbonation [16,17,25], freezing-thawing cycles [16,26], abrasion [7] or high temperatures [27], which provides greater durability.

Regarding the resilience, it is also known that the durability of concrete structures is often compromised by the presence of cracks while exposed to an aggressive environment [2,3,28,29–31]. In this context, EAFS concrete capacity is limited by its brittleness. Increasing the ductility of concrete enhances the postcracking behavior [31–36], therefore, it contributes to enhance structural resilience, requiring less frequent repair works. In this work steel and synthetic fibers have been added to improve EAFS concrete post-cracking behavior [9,32,37–42].

The behavior of fiber-reinforced concrete depends on the fibers characteristics, concrete properties and the matrix-fiber interaction [32,43–48]. The addition of fibers has hardly any effect on the compression strength and improves slightly the tensile strength [32,39,40,49]. However, the postcracking performance is improved significantly and particularly when steel fibers are added [41,50–52].

Despite fiber-reinforced EAFS concrete is experimentally well-studied at a laboratory-scale, its application in structural elements is very limited yet [7]. It has been used in elements such as pavements, foundations or retaining-walls [4,7,17,39,53], but its utilization in structural elements along with reinforcement is still a challenge. A reliable Finite Element Method (FEM) which models EAFS concrete, fibers and reinforcement bars, can facilitate to use it in engineering applications. In this study, fibers bridging phenomena and plain concrete fracture is modeled through interface elements (triangular finite elements with high aspect ratio). The constitutive model applied, isotropic damage model, in the interface elements have to describe the fracture of concrete and the pullout of fibers in EAFS concrete [54-59]. In this work, the presented numerical framework for fiber-reinforced EAFS concrete in [32] is extended to structural elements. However, to our knowledge, it remains limited the coupling of interface elements with reinforcing bars in EAFS concrete structures.

Reinforcement bars are embedded in concrete in such a manner that provides tensile strength for concrete, which make reinforced concrete appropriate to use as a structural material. Reinforcing steel bars usually show a linear elastic behavior in tension up to a yielding strain and it is followed by hardening behavior up to an ultimate stress. In this work, the behavior of structural steel is modeled through the Menegotto-Pinto constitutive model [60–64] and steel bars are discretized through one dimensional truss elements. The introduction of interface elements requires a new approach to introduce shear and longitudinal reinforcement, which permits crack propagation and keeps the constraining conditions. Unlike previous works [65,66], in this approach truss elements are inserted in an unstructured mesh.

Having studied fibers performance in EAFS concrete through interface elements in [32], the challenge in this study is to integrate interface elements with longitudinal and shear reinforcement to model structural elements. The aim of this work is presenting a FEA which provides valuable information about the cracking in structural elements which is not possible to estimate trough experiments. This information might be used to study the durability of the structure due to chemical attacks or the reduction in strength of the concrete. The proposed numerical model solves the bottleneck problem of fiber-reinforced EAFS concrete to be applied in engineering problems.

The article is structured as follows. Section 2 presents the dosage of the studied concrete, the implemented FEM and the description of the tests. In Section 3 the numerical model is validated through a simplified test and full-scale specimens made with fiber-reinforced

Table 1
EAFS concrete dosage (kg/m^3).

	IISC	IISC-M	IISC-S
Limestone: $\phi < 1.2\,mm$	950	950	950
EAFS: $\phi < 4\,mm$	550	550	550
EAFS: $\phi = 4 - 12\,mm$	750	750	750
Synthetic fibers	-	-	4.5
Steel fibers	-	40	-
CEM II/B-S 42.5 R	330	330	330
Additives	5.3	5.3	5.3
Water	170	180	185

EAFS concrete and the experimental and numerical results are discussed. Lastly, the conclusions and future perspective are presented in Section 4.

2. Material, tests and Finite Element Model

2.1. EAFS concrete mixes

In this research study, self-compacting slag concrete was used to cast the specimens. Table 1 presents the dosage of the studied three mixes, where the main difference is the addition of fibers, and they are identified as i) IISC: Plain concrete ii) IISC-M: Steel-fiber reinforced concrete iii) IISC-Y: Synthetic-fiber reinforced concrete.

In the three mixes CEM-II (Portland-slag cement) is used with a compression strength of 42.5 MPa at 28 days. Portland cement is partially replaced with blast furnace slag, which reduces the environmental impact of concrete. As most of modern concrete, super-plasticizers are added to improve its workability [67]. Cement-admixture compatibility depends on factors such as mineralogical composition of aggregates, fineness or chemical and structural composition of admixtures [22].

The distinguishing fact of the employed mixes is the substitution of natural aggregates with EAFS. The main advantages of EAFS respect to natural aggregates are its roughness, angularity, toughness-strength-stiffness, abrasion resistance, density, and chemical basicity [7,40]. They were obtained crushing slags produced at a certain stage of steel-making process in an electric arc furnace. Two different grading were used i) Gravel-sized EAFS (4–12 mm) ii) Sand sized EAFS ($<$ 4 mm). Considering the high energy required to crush slags, limestones were added as fine aggregates ($<$ 1.2 mm) to get the required cohesiveness of the paste [22,68].

Regarding the fibers, steel and synthetic fibers were added to improve the postcracking behavior (0.5% of the total volume). It was concluded that this amount of fibers had negligible impact in the workability in [40]. Table 3 illustrates fibers properties required by the implemented constitutive models. Hooked-end steel fibers increases the anchoring of the fibers, requiring higher loads to be pulled out. This fact must be considered in the softening law employed to describe the bridging phenomena. It is also assumed that they are uniformly and randomly distributed.

The performance of steel and synthetic of fibers in EAFS concrete was deeply studied in our previous work [40]. The pull-out test carried out showed a good adhesion of the fibers. It should be noted also the superior performance of steel fibers due to the gained toughness [32,40].

A detailed analysis of the mixes can be found in [7,22,32,40,68,69] where EAFS concrete dosage and fibers performance is extensively studied.

2.2. Tests

The presented tests are carried out to provide further evidences for fiber reinforced EAFS concrete and to validate the developed numerical model for bar and fiber-reinforced EAFS concrete. These tests complement the tests presented in our previous work [32].

2.2.1. Full-scale test set up

Concrete beams for flexural using were tested to assess the performance of the presented FEM. The experimental program consisted of rectangular beams with a cross-section of 200 $\times$300 mm^2 (width x height) and length of 4400 mm. The beams were supported at both ends and the span was of 4000 mm. The beam was subjected to a four-point load, according to Fig. 1, with a distance between the loads of 1000 mm.

The specimen was designed to evaluate the performance of fibers. To this end, the longitudinal reinforcement consisted of 2ϕ16

Table 2
Material properties to model Bulk elements.

	IISC	IISC-M	IISC-Y
Direct tensile strength, f_{td} (MPa)	4.25	3.77	3.66
Compressive strength, f_c (MPa)	59.66	53.09	46.08
Young's modulus, E_c (MPa)	40.1×10^3	34.7×10^3	31.6×10^3
Plain concrete fracture energy, G_F (N/mm)	0.137	0.137	0.137
Poisson's ratio, ν	0.23	0.22	0.22

Table 3
Fibers properties to model Interface elements.

	Steel fibers	Synthetic fibers
Tensile strength (MPa)	1200	400
Young's modulus (MPa)	210×10^3	6×10^3
Poisson's ratio	0	0
Fiber volume content (%)	0.5	0.5
Fiber length/diameter (mm/mm^2)	35/0.55	35/0.93
Fiber shape	Hooked-end	Dimpled-surface

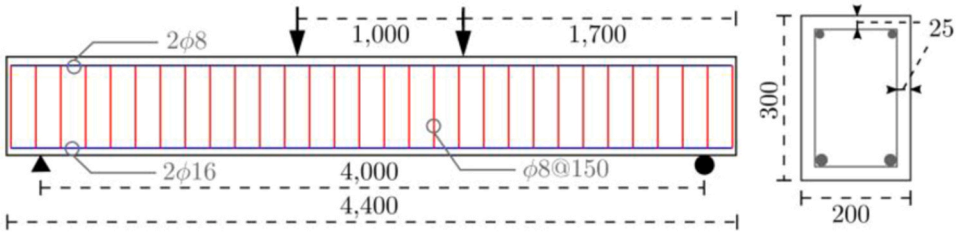

Fig. 1. Flexural beam set up.

Fig. 2. Flexural beam set up.

bars at the bottom part while 2ϕ8 bar were placed at the top part. The transverse reinforcement consisted of ϕ8 hoops spaced 150 mm. Fig. 1 shows the detailed settings of the beam.

The tests were carried out controlling the deflection at three different ranges:

1. 0.5 mm/min was applied until the first cracks were detected.
2. 1 mm/min was applied while the cracking.
3. 2 mm/min was applied since cracks were generated up to the end of the test.

The load, support settlements and the strain at the mid-span were measured during the tests as it is showed in Fig. 2.

2.2.2. Full-scale FEM inputs

Table 2 presents the properties of the three mixes required to define the inputs of constitutive models. These inputs define the behavior of bulk elements (elastic law) and interface elements (softening law). The Elastic modulus (E_c), compression strength (f_c) and Poisson's ratio (ν) are defined by compression tests [70,71], while fracture energy (G_F) was defined through three-point bending tests [72]. These test were carried out following the European standards. However, the tensile strength (f_{td}) was defined by direct tensile

tests (Dog-bone tests), which is a non-standardized test. It is worth noting that direct tensile test gives more suitable tensile strength than the widely used Brazilian test as it was studied in [32]. A thorough assessment of these properties and a detailed description of the tests is presented in [32].

Steel and synthetic fibers properties are introduced in Table 3. These properties are used to define the last two terms of the softening law, Eq. (2), which is used to define the bridging phenomena for the mixes IISC-M and IISCY.

Table 4 presents the parameters required by the Menegotto-Pinto constitutive model to describe the behavior of the structural steel. The parameters of the model (R_0, a_1, a_2, a_3 and a_4) for structural steel are assigned based in the values proposed in [60,62].

2.3. Finite element model

2.3.1. Fibers and fracture modeling: interface elements

A method based on the introduction of interface elements between elements of the mesh (bulk elements) is used to capture the cracking phenomena. These interface elements are the responsible to model the kinematics associated to discontinuities, so that the crack formation can grow through the boundaries of the bulk elements [54,56,57]. The domain is discretized with an unstructured mesh to capture the crack paths accurately and to avoid being influenced by the mesh orientation. Then, pairs of triangular finite elements with high aspect ratio are inserted between bulk elements of the conventional mesh. Fig. 3 illustrates the different stages to introduce the interface elements in a mesh.

Based on the governing behavior of the concrete (plain concrete or fiber-reinforced concrete), the tensile damage model is adjusted. The damage criterion, ϕ, is determined based on the equivalent stress, $\tilde{\sigma}$, and stress-like internal variable:

$$\phi = \tilde{\sigma} - q(r) \leq 0 \tag{1}$$

The softening law is defined based on the strain-like internal variable (r) as:

$$q(r) = \left(f_{t,com} - t_1\right) \quad e^{\frac{-r}{\omega_{ref}}} + t_1 \frac{\omega_u - r}{\omega_u} + t_2 \quad r \quad e^{c_1 - c_2 r} \tag{2}$$

The tensile strength of the composite, $f_{t,com}$, is determined through the direct tensile tests (Dog-bone test) instead of the widely used Brazilian test. t_1, t_2, c_1, and c_2 are the fitting coefficients and they are defined fitting with the experimental curves of the three-point bending test presented in [32]. The reference crack opening displacement ω_{ref} is derived from the fracture energy G_F computed in the three-point bending test made with plain concrete.

$$\omega_{ref} = \frac{f_{t,com}}{G_F} \tag{3}$$

As homogeneous distribution of fibers is considered, fibers are pulled out when half of its length L_f is displaced. Therefore, the ultimate crack opening, ω_u, can be defined as

$$\omega_u = \frac{L_f}{2} \tag{4}$$

Eq. (2) presents the softening behavior of fiber-reinforced EAFS concrete proposed by [48] to model plain concrete or fiber-reinforced concrete fracture. The first expression of Eq. (2) is related with the fracture of plain concrete, while the last two are associated with the fiber-reinforcement (bridging phenomena). The last two terms are not considered when plain concrete is modeled. The second term considers the frictional features during the pullout of fibers. The last expression is associated with the additional anchorage that some types of fibers could have owing to their shape, such as the hooked-end fibers used in this research.

A detailed explanation of the implementation of interface elements and damage model was presented in a previous work [32]. They were validated with experimental data, which proves that the FEM is adequate to model steel or synthetic fiber-reinforced EAFS concrete.

2.3.2. Reinforcing bar discretization: Truss elements

Reinforcement can be modeled as a smeared overlay or with truss elements. Considering the introduction of interface elements to model concrete fracture, truss elements are selected as the most suitable option. It avoids inducing preferential cracking paths and also

Table 4
Full-scale beam reinforcement inputs.

INPUT	Reinforcement
Elastic stress, σ_y (MPa)	650
Young's modulus, E_y (MPa)	250×10^3
Hardening modulus, E_0 (MPa)	5×10^3
Sup longitudinal reinf. area (mm^2)	100
Inf. longitudinal reinf. area (mm^2)	402
Shear reinf. area (mm^2)	100
Curvature, R_0	20
Parameters a_1, a_2, a_3 and a_4	0, 0, 18.5 and 0.15

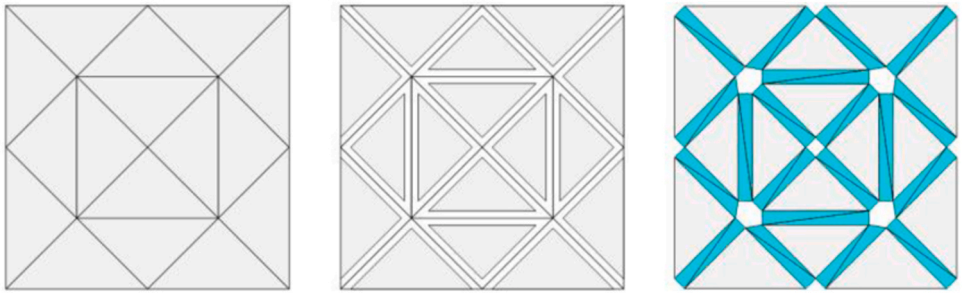

Fig. 3. Interface elements insertion.

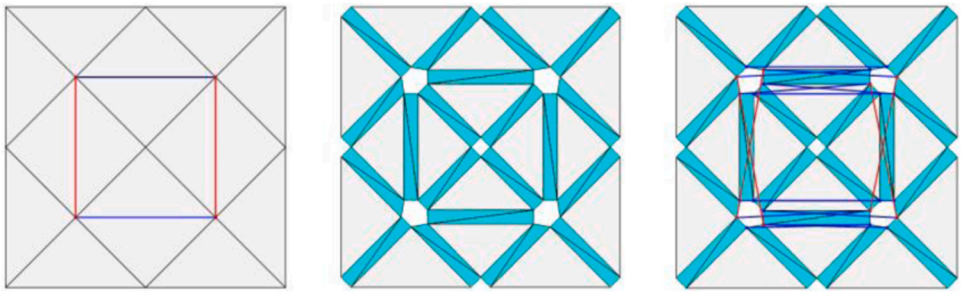

Fig. 4. Reinforcement discretization.

allows discrete cracks crossing the reinforcement.

Fig. 4 shows the introduction of longitudinal (blue color) and shear reinforcement (red color). The number of interior nodes is increased due to the introduction of interface elements. Consequently, linear elements, which had one starting point and end point in the original mesh, have to be redefined once introducing interface elements. The new discretization has to connect the highest number of nodes to maximize the numerical stability and to ensure the restraining conditions [65].

In this approach, the longitudinal (or flexural) reinforcements are divided into a sufficient number of truss elements that realizes the above-mentioned premise. This approach is intuitive for structured meshes, where the number of starting and end nodes are the same. However, it must be particularized for unstructured meshes to suit to the number of starting and end nodes, which might be different. The number of elements used is defined by the maximum number in which the starting or end nodes are partitioned. This number of elements ensure that all the nodes are constrained and linked. The cross section of the new elements are computed by splitting the total area of the longitudinal reinforcement. Concerning the transversal (or shear) reinforcements, they can be simplified by two linear elements forming a cross. This streamlining optimizes the computational cost while it provides enough restraint to the model [65].

2.3.3. Menegotto-Pinto constitutive model

The constitutive model selected to model the behavior of steel reinforcement-bars is Menegotto-Pinto plasticity model [60], which is widely used to simulate structural steel [61–64]. The used model is a bilinear model where the first part is a line defined by the elastic

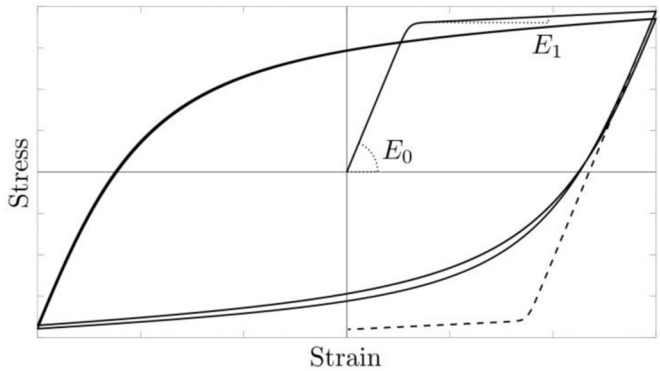

Fig. 5. Menegotto-Pinto uniaxial constitutive model for steel.

modulus (E_0) and yield stress (σ_y) of the steel while the second line is defined by the slope or hardening modulus (E_1). In Fig. 5 shows the bilinear model in the first loading cycle.

Once the yielding stress (σ_y) is exceeded, the microstructure of the material is modified. This dislocation generates internal stresses that influences on the stress-strain behavior what is known as Bauschinger effect. Hence, the yield strength is lower for reversed loading direction when yielding limit is overtaken. Fig. 5 shows the curve without considering the Bauschinger effect (dashed line) and the curve considering it.

The stress state (σ) is computed as

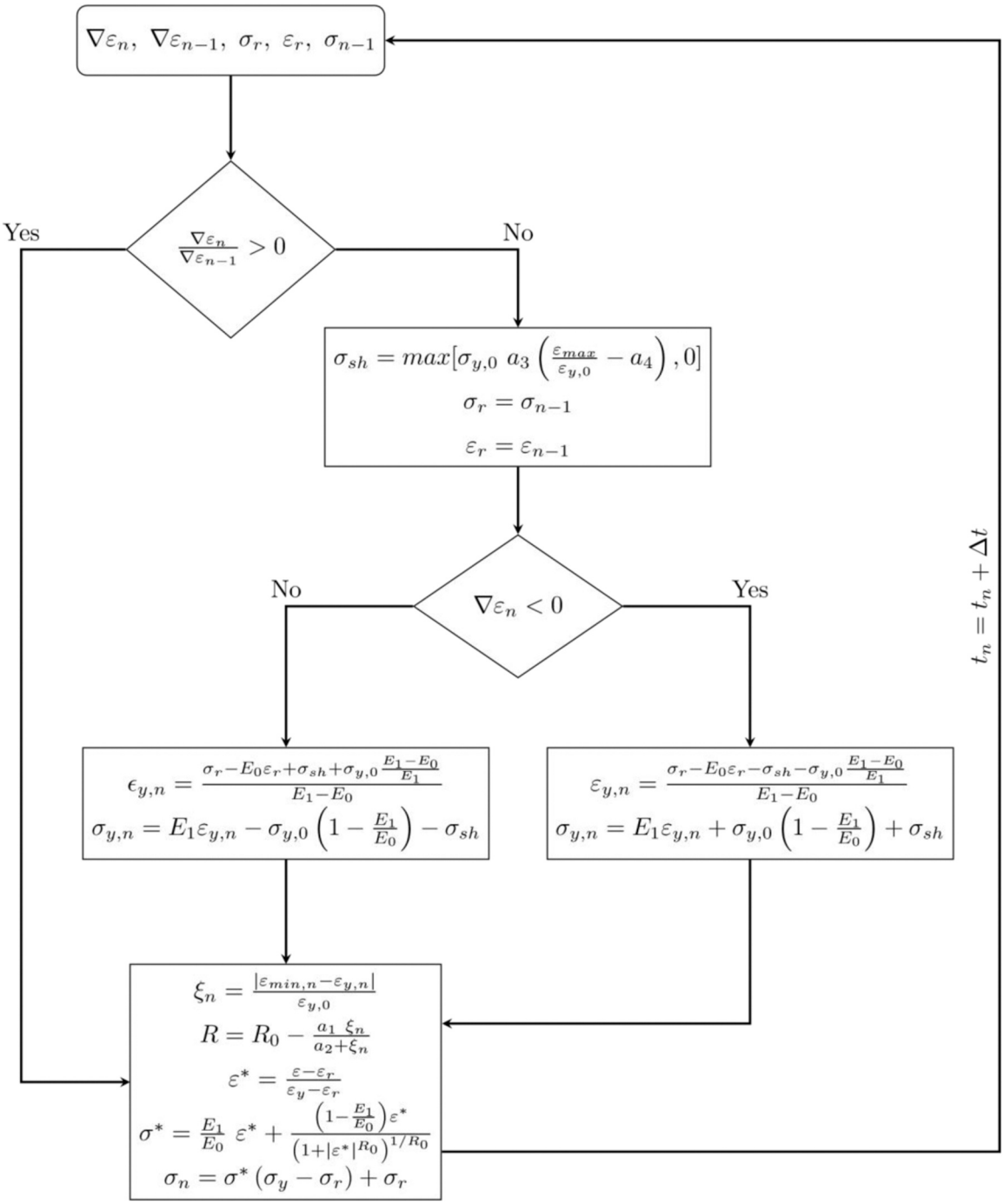

Fig. 6. Flowchart of the algorithm implemented for Menegotto-Pinto constitutive model.

$$\sigma = \sigma^{*}\left(\sigma_{y} - \sigma_{r}\right) + \sigma_{r} \tag{5}$$

where σ_r is the stress at the last reversal time. The normalized stress (σ^*) is defined as

$$\sigma^{*} = \frac{E_1}{E_0}\varepsilon^{*} + \frac{\left(1 - \frac{E_1}{E_0}\right)\quad \varepsilon^{*}}{\left(1 + \left|\varepsilon^{*}\right|^{R_0}\right)^{1/R_0}} \tag{6}$$

$$\varepsilon^{*} = \frac{\varepsilon - \varepsilon_r}{\varepsilon_y - \varepsilon_r} \tag{7}$$

where ε^* is the normalized strain, ε_r is the strain at the last reversal time and R_0 is the curvature at the first loading step. The transition curve after the first reversal is determined by the curvature:

$$R = R_0 - \frac{a_1\quad \xi_n}{a_2 + \xi_n} \tag{8}$$

where a_1 and a_2 are parameters determined experimentally and ξ_n is the ratio of the maximum plastic strain over the initial yield strain. The parameter R introduces the Bauschinger effect which improves significantly the accurateness of the results [73–75].

Fig. 6 illustrates the flowchart of the Menegotto-Pinto constitutive model. After initializing variables ($\sigma_r = \varepsilon_r = 0$), it is determined if the loading direction is the same as in the previous loading step. In case of changing the loading direction, the isotropic strain hardening is determined by computing the new isotropic stress (σ_{sh}), given by

$$\sigma_{sh} = \sigma_{y,0}\quad a_3\quad \left(\frac{\varepsilon_{\max}}{\varepsilon_{y,0}} - a_4\right) \tag{9}$$

where a_3 and a_4 are parameters determined experimentally and ε_{max} is the maximum absolute strain at the instant of strain reversal and $\sigma_{y,0}$ and $\varepsilon_{y,0}$ are the initial yield stress and strain. Subsequently, the loading direction is identified (tensile or compression) and the coordinates of the intersection point of the two asymptotes are defined (σ_y, ε_y). Once these variables are defined, the stress state can be calculated (σ_n, ε_n) using Eq. (5). This procedure is repeated in every loading step.

3. Experimental and numerical results and discussion

3.1. Finite element analysis result

In this section, first a simplified beam (Longitudinally-reinforced concrete beam) is simulated to validate the performance of bar-reinforcement modeling approach presented in Section 2.3. Next, the results of the FEM are compared with four-point flexural tests made with the three mixes presented in Table 1.

3.1.1. Longitudinaly-reinforced concrete beam (Small-scale test)

The three-point bending beam tested in *Ruiz et al.* [76] is modeled to validate the presented model for reinforcement. This beam is made with plain concrete and only reinforced with longitudinal bars (4ϕ2.5). The dimensions of the beam are 1350 ×300×50 mm and the detailed set up is shown in Fig. 7.

Triangular elements of 10 mm are used to mesh the beam and it is remeshed in the central zone, where the fracture is expected, with elements of 5 mm. The height of the introduced interface elements is 0.001 mm. The beam is modeled as a 2D plane-stress problem, while the reinforcement bars are considered 1D element and perfectly bonded. The model is defined by three constitutive models (Bulk elements, interface elements and reinforcement). Table 5 presents the inputs required by the applied constitutive models. The beam is made with plain-concrete so a tensile-damage model for plain concrete is implemented in the interface elements [32].

Fig. 8 compares the experimental results presented in [76] with the computed numerical results. The numerical and experimental

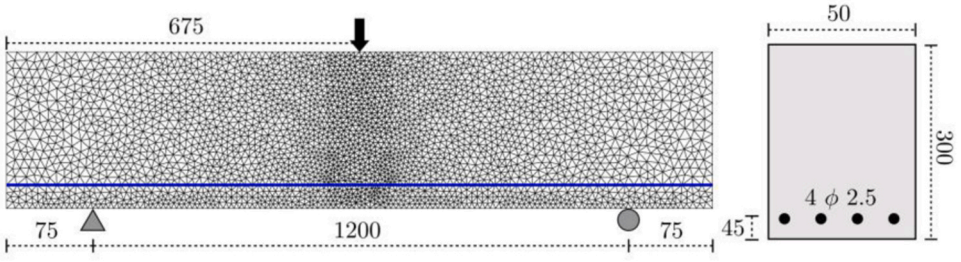

Fig. 7. Longitudinally reinforced beam set-up (mm).

Table 5
Longitudinally reinforced beam FEM inputs.

Bulk elements	
Young's modulus (MPa)	29×10^3
Compressive strength (MPa)	39.5
Poisson's ratio	0.2
Interface elements (Plain concrete)	
Young's modulus (MPa)	29×10^3
Hardening modulus, E_0 (MPa)	0
Poisson's ratio	0
Tensile strength (MPa)	3.8
Fracture energy (N/mm)	0.0625
Reinforcement	
Young's modulus (MPa)	162 ×103
Tensile strength (MPa)	587
Section (mm2)	19.63
Strain hardening ratio	0
R0	20
a1, a2, a3 and a4	0, 0, 18.5 and 0.15

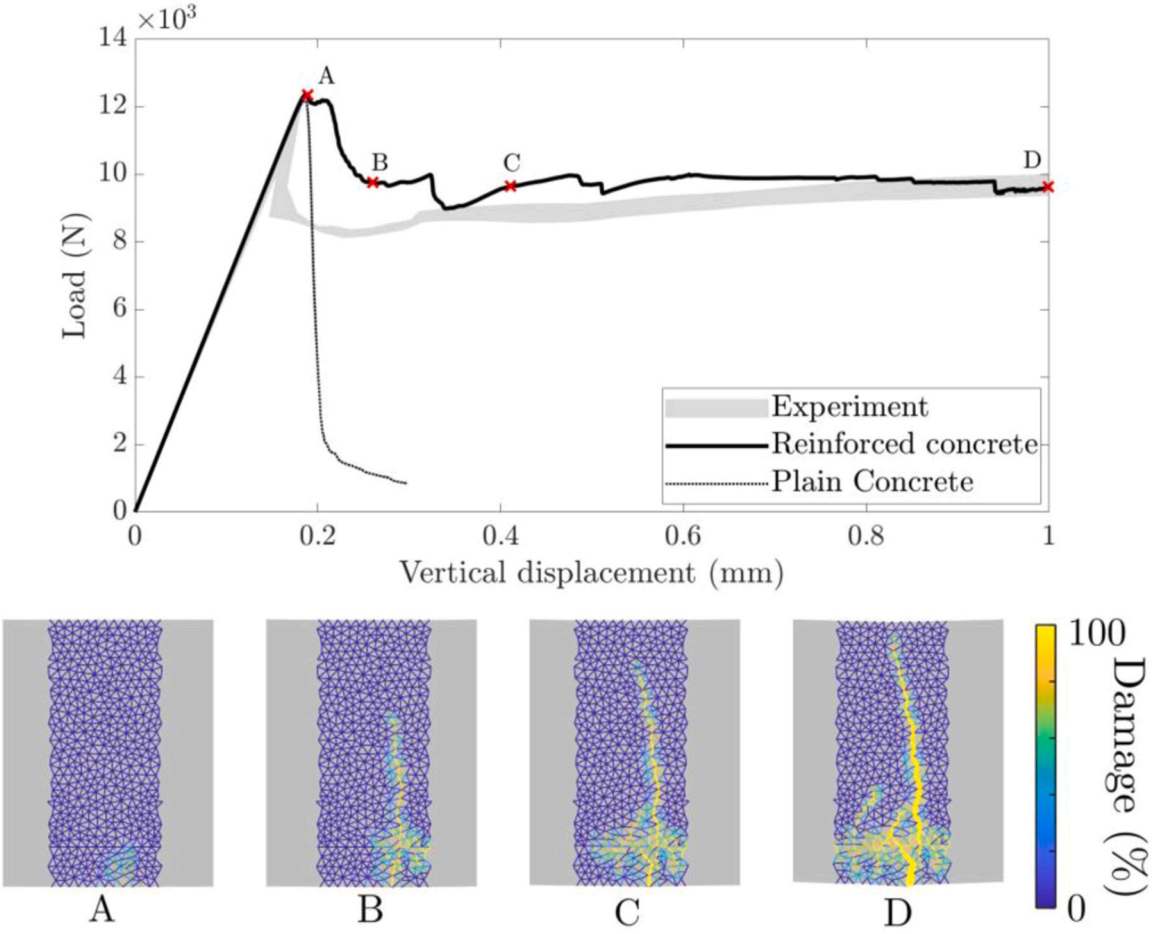

Fig. 8. Reinforced concrete beam load/displacement curve and damage development.

curves have a strong resemblance during the prepeak stage. At the end of this stage (Point A), the crack is generated and interface elements start to damage as shown in the bottom part of the Fig. 8. Despite there is a slight difference with the experimentation, the load dropping just after the generation of the crack can also be assumed as captured by the numerical model. Beyond this point the experimental range and the numerical curve match well enough. In this range the concrete is degraded and the slope of the structural curve depends strongly on the reinforcement.

After Point A the beam is loaded up to failure. The development of the crack is more visible as it is reported in Fig. 8, however, in-situ studies of the crack are highly challenging due to the scale of the phenomena. The cracks are developed in the central zone of the beam where interface elements are introduced. The crack development differs markedly from plain concrete beams analyzed in [32]. In the case of plain concrete elements, all the damage is localized in a narrow band and one main crack is developed [32]. In bar-reinforced concrete initially, the damage is mainly developed in a narrow band as in plain concrete. Afterwards, the damage develops along the reinforcement through orthogonal microcracks in the concrete surrounding the reinforcement bar. The developed microcracks between the bar and concrete could cause the debonding of the reinforcement. Fig. 8 shows the development of damage at the pointed displacements (Point A, B, C and D).

Regarding the reinforcement, the developed model allows knowing the stresses at the reinforcement at different loading steps. Fig. 9 illustrates the reinforcement crossing the interface elements and shows the stresses at loading point D.

3.1.2. Bar reinforced EAFS concrete beam (IISC)

The studied beam in this section is made with the mix IISC (without fibers) and the inputs required by the numerical models are reported in Table 2, while the geometry is defined in Fig. 1. The beam is meshed with triangular elements of 20 mm height and interface elements of 0.001 mm height are introduced along the beam. The same discretization is used for the beams made with IISCM and IISC-Y.

Fig. 10 illustrates the load/displacement curve at the middle point of the beam. The numerical model shows greater stiffness at the first stage up to concrete starts damaging (displacements about 2.5 mm). At this point, the slope of the curve changes which indicates that concrete starts damaging and cracks developing. After this point, the strength of the beam in the tensile part is mainly due to the steel bar, giving rise to change in the slope of the curve. The numerical curve is less steep than the experimental curve which means that the model is less stiff than the reinforced beam. Lastly, the maximum load is quite similar in both cases, although the experimental curve reaches its highest value earlier. Even considering these minor differences, the numerical results match well with the experimental curve.

Examining the damage level of intermediate elements, the degradation of concrete elements, which is related with concrete fracture, can be thoroughly studied. Fig. 10 shows the evolution of the damage by three snapshots at the indicated loading points. The damage is located in preferential vertical bands, which is the main difference compared to the beams made with fibers as it is shown in the next sections. In the first stage the damage is concentrated in the middle part of the beam and then it is spread along the beam. Comparing the snapshots at the displacement of 10 mm and 30 mm, the damage level increase slightly while the vertical displacement grows significantly. Therefore, the beam is damaged in the first loading steps while at later stage the deflection is more evident. In the last two snapshots, the damaged bands at the corners are not as clear as in the central part because it is less damaged. Moreover, they have an inclination due to the shear stresses, in contrast to the vertical cracks developed in the central part (pure bending conditions).

3.1.3. Steel fiber and bar -reinforced EAFS concrete beam (IISC-M)

The analyzed beams is made with steel fiber-reinforced concrete (IISC-M). The inputs of the bulk and interface elements are defined in Table 2 and Table 3 respectively. The geometry and the steel bar-reinforcement is the same as in the beam made with IISC.

Fig. 11 compares the experimental and numerical load/displacement curves of the mix reinforced with steel fibers. The numerical and experimental curves follow a similar pattern as the IISC beam. At the first stage the numerical curve shows a higher stiffness than

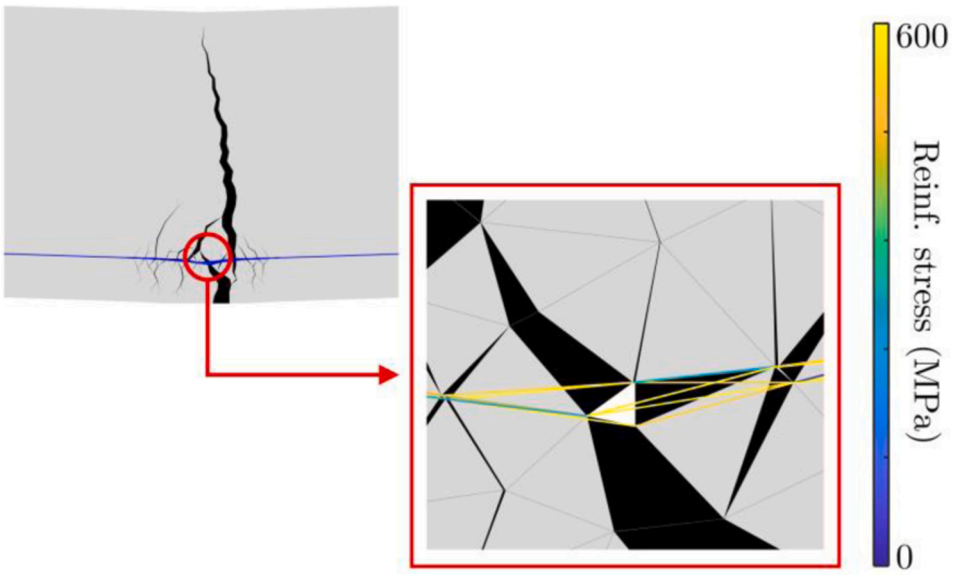

Fig. 9. Reinforcement bars at stage D.

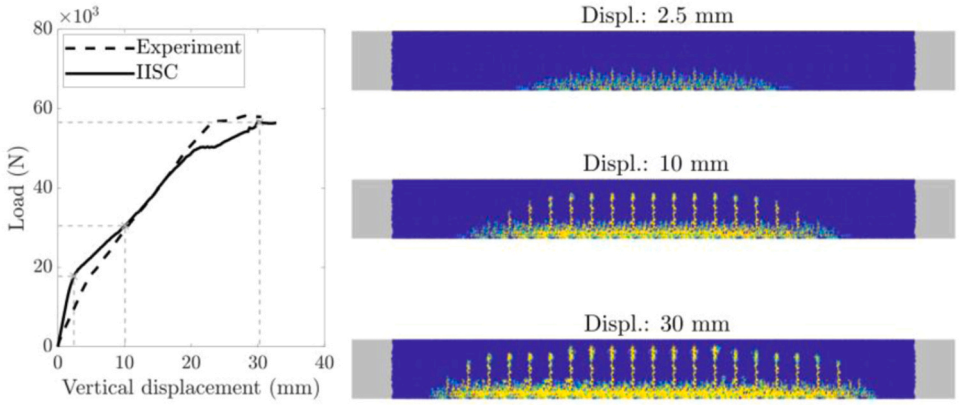

Fig. 10. Load/deflection curve and damage development of the beam IISC.

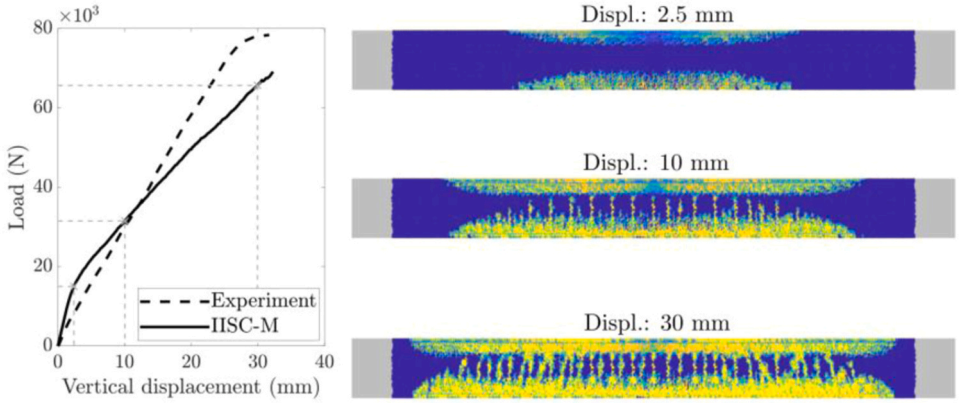

Fig. 11. Load/deflection curve and damage development of the beam IISC-M.

the experimental one. After the failure of concrete in the tensile part, the modeled beam is less stiff than the real beam and the slope of the numerical curve is smaller. In this case, the numerical failure load does not get the load of the experiment and the difference is about 11.5%.

Fig. 11 shows the evolution of the damage in the interface elements at the pointed loading steps. The fracture mode of the beam reinforced with steel fibers is completely different to the one without fibers. The damage is spread along the beam due to the addition of fibers and the beam is more fractured, which redistributed the stresses. At the first stages, the cracks are separated by 150 mm as in the IISC beam. The early cracks are generated in the flexural part of the beam and they are developed vertically. However, the cracks located closer to the supports tend to incline due to the shear stresses. However, secondary cracks are generated between the initial cracks in the other two snapshots, which differ remarkably from the beam made with IISC.

It can be concluded that IISC-M beam shows greater strength than the IISC. The beam IISC-M is more fractured and requires more energy to get this damage level. Steel fibers are the responsible of spreading the damage along the beam due to the hardening behavior. This performance is aligned with the conclusions presented in [32] for steel fibers.

3.1.4. Synthetic fiber and bar -reinforced EAFS concrete beam (IISC-Y)

The beam made with the mix IISC-Y is also modeled following the presented framework and the inputs of the model are presented in Table 2 and Table 3. Fig. 12 compares the load/displacement curves of the experiment and the simulation. The numerical model fails close to the vertical displacement of 35 mm. After this point the numerical model shows anomalous behavior due to the high damage range of the interface elements. The numerical curve shows higher rigidity than the experimental curve in the first loading steps following the pattern of the other mixes. However, the stiffness decreased becoming the numerical curve less stiff than the real beam up to the failure point. This behavior is aligned with the behavior of the other mixes.

The damage is more distributed than the beam made with the mix IISC, however, it is not as distributed as the mix IISC-M. This is aligned with the conclusions presented in [32]. Fig. 12 shows the evolution of the damage at the loading steps pointed in Fig. 12. In this case, it is not developed a secondary region of damaged elements as in the case of the mix IISC-Y. In the middle zone of the mix (pure bending) the damage regions are vertical while close to the supports the damaged regions are inclined due to shear stresses. The

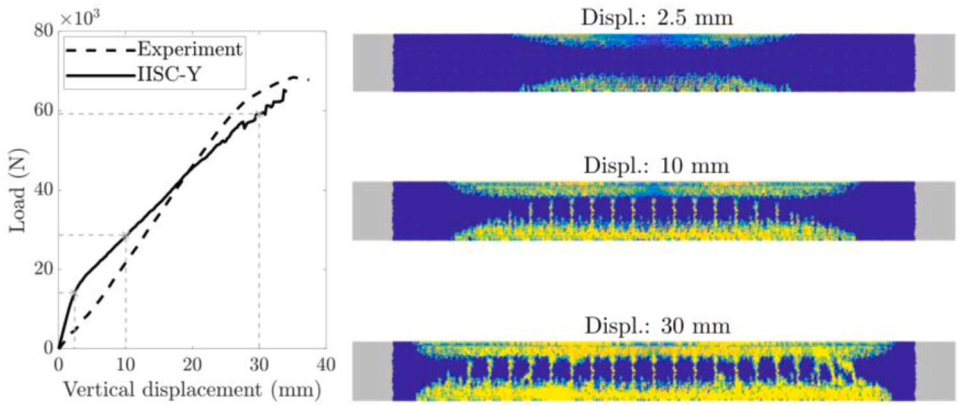

Fig. 12. Load/deflection curve and damage development of the beam IISC-Y.

damaging of the beam reinforced with synthetic fibers shows an intermediate scenario between IISC and IISC-M.

3.1.5. Assesing structural performance using numerical results

The numerical results provide more data to asses the performance of fibers which is difficult or almost impossible to get from the experiments. Table 6 illustrates interesting data computed from the finite element model at the deflection of 20 mm. The mix IISC-M requires a greater load to get the indicated displacements. The beams reinforced with fibers showed greater number of damaged elements and damage level. These facts indicate that the damage is more distributed along the beam compared to the beam made with IISC.

The maximum cracks depths are very similar in the three cases, while the average depth of the crack is slightly different at the deflection of 20 mm. Nevertheless, the crack mouth opening displacement (CMOD) shows greater differences between the mixes. The improvement is remarkable when steel fibers are added. The maximum and mean CMOD are reduced in 17.1% and 12.3% compared with the mix IISC.

Table 7 illustrates some useful data to analyze concrete fracture at the loading step of 35 kN. As it was expected, the mix IISC-M shows the minor deflection at the middle point. The fiber-reinforced concrete beams are significantly more damaged than the mix IISC. The damage level and the number of damaged elements are more than double to the mix without fibers. These facts mean that the damage is more distributed along the beam and higher loads are required to get these damage level. Therefore, adding fibers make full use of the capacities of EAFS concrete.

The maximum crack depth of IISC and IISC-Y are very close, while the mix IISC-M shows superior performance. However, the difference between the mixes is more evident when the mean depth of the cracks is analyzed. The mean depth of the cracks is 12.5% and 6.2% less in IISC-M and IISC-Y, respectively. Regarding CMOD, the results computed for the mixes IISC and IISC-Y are very similar, while the mean and maximum values of CMOD are considerably better for the mix reinforced with steel fibers. The steel fibers compared to IISC improves the mean and maximum CMOD in 29.3% and 12.7%, respectively.

4. Conclusions

The advantageous properties of fiber-reinforced EAFS concrete are well studied at material scale but its application in structural elements is limited yet. A FEA provides an in depth knowledge of the mechanical behavior and it can facilitate its usage in structural elements.

To take advantage of this advantageous performance in structural elements, a finite element model is presented. Plain and fiber-reinforced EAFS concrete fracture and bridging phenomena are modeled through interface elements. Longitudinal and shear reinforcement is discretized through truss elements and the implemented constitutive model is the Menegotto-Pinto model. The presented finite element model is validated through three full-scale beams made with plain EAFS concrete, steel fiber- and synthetic- fiber rein-

Table 6
Crack and damage state at deflection 20 mm.

	IISC	IISC-M	IISC-Y
Load (kN)	47.89	49.53	45.60
Damage (%)	18.69	45.89	42.11
Damaged elements	7334	18,139	16,509
Max. depth (mm)	219.93	219.38	219.85
Mean depth (mm)	86.46	82.37	82.41
Max. CMOD (mm)	0.1804	0.1495	0.2188
Mean CMOD (mm)	0.0314	0.0274	0.0284

Table 7
Crack and damage state at load step 35 kN.

	IISC	IISC-M	IISC-Y
Deflection (mm)	12.7	12.0	14.0
Damage (%)	15.08	37.4	36.5
Damaged elements	6099	15,558	14,997
Max. depth (mm)	219.28	216.24	219.58
Mean depth (mm)	86.88	76.15	81.46
Max. CMOD (mm)	0.1272	0.0894	0.1427
Mean CMOD (mm)	0.0198	0.0166	0.0194

forced EAFS concrete.

The conclusions of this work can be summarized as follows:

1) The proposed FEM provides valuable information to understand the fracture mechanics of structural elements made with fiber- and bar- reinforcement. The FEM framework provides quantities of interest such as CMOD and crack depth for real-life engineering applications, which otherwise are only available in simple structures in laboratory environments. Other parameters such as the damage rate, are not possible to define experimentally, which facilitates understanding damage evolution and applying corrective measures in the damaged regions.
2) A discretization method is proposed for linear elements in unstructured meshes. The discretization method for the reinforcement does not condition crack propagation along the interface elements.
3) These tests evidence that mixes reinforced with fibers resist higher loads, which is aligned with the conclusions of our previous work carried out in specimen without bar-reinforcement.
4) The FEA reveals that fiber-reinforced EAFS concrete is more damaged and the damage is spread along the beam. Fiber-reinforced EAFS concrete beams show lower values on crack mouth opening displacement. It should also be noted the effects of steel fibers at the postcracking stage. The damage is more distributed along the beam, which enables to get greater loads.

The presented numerical framework provides a starting point to apply fiber-reinforced EAFS concrete in structural elements and it has potential for improvement. Future research into fiber-reinforced EAFS concrete structures should focus on assessing its performance in other structural elements to make it widely used. Furthermore, while this work study the fracture mechanics due to static loads, dynamical tests are required to gain more insight into the behavior of fiber-reinforced EAFS concrete in structural elements. The proposed FEA could be improved considering new physical phenomena, such as contact between reinforcement and concrete reinforcement, or non-uniform fiber distribution.

CRediT authorship contribution statement

Vanesa Ortega-López: Formal analysis, Funding acquisition, Project administration, Resources. **Amaia Santamaria:** Formal analysis, Funding acquisition, Validation. **Miquel Aguirre:** Conceptualization, Funding acquisition, Software, Writing – review & editing. **Aratz Garcia Llona:** Conceptualization, Data curation, Software, Visualization, Writing – original draft. **Ignacio Piñero:** Formal analysis, Validation.

Declaration of Competing Interest

The authors declare that they have no known competing financial interests or personal relationships that could have appeared to influence the work reported in this paper.

Data availability

Data will be made available on request.

Acknowledgment

The authors wish to express their gratitude to the following entities for having funded by MCIN/AEI/10.13039/501100011033 and by “ERDF A way of making Europe”, by the “European Union” [PID2020–113837RB-I00; PID2021–124203OB-100; RTI2018–097079-B-C31, PID2021–124203OB-100]; the Junta de Castilla y León (Regional Government) and ERDF [BU119P17, UIC-231]; the University of Burgos [Y135.GI]; the Basque Government [IT1619–22 SAREN research group]. We would like to thank CHRYSO and HORMOR for supplying the materials used in this research. This work has been partially supported by a Maria Zambrano research fellowship at Universitat Politecnica de Catalunya funded by Ministerio de Universidades.

References

[1] Amani, A.M. Ramezanianpour, M. Palassi, Investigation on the sustainable use of electric arc furnace slag aggregates in eco-friendly alkali activated low fineness slag concrete as a green construction composite, J. Clean. Prod. 307 (2021) 127257, https://doi.org/10.1016/j.jclepro.2021.127257.
[2] W. Fan, Y. Chen, J. Li, Y. Sun, J. Feng, H. Hassanin, P. Sareh, Machine learning applied to the design and inspection of reinforced concrete bridges: resilient methods and emerging applications, Structures 33 (2021) 3954–3963, https://doi.org/10.1016/j.istruc.2021.06.110.
[3] P. Hajek, Concrete structures for sustainability in a changing world, Procedia Engineering 171 (2017) 207–214, the 3rd International Conference on Sustainable Civil Engineering Structures and Construction Materials Sustainable Structures for Future Generations. doi:10.1016/j.proeng. 2017.01.328.
[4] F. Maghool, A. Arulrajah, Y. Du, S. Horpibulsuk, C. Chinkulkijniwat, Environmental impacts of utilizing waste steel slag aggregates as recycled road construction materials, Clean. Technol. Environ. Policy 19 (2017) 949–958, https://doi.org/10.1007/s10098-016-1289-6.
[5] P.J. Monteiro, S.A. Miller, A. Horvath, Towards sustainable concrete, Nat. Mater. 16 (7) (2017) 698–699, https://doi.org/10.1038/nmat4930.
[6] C. Wang, J. Xiao, Evaluation of the stress-strain behavior of confined recycled aggregate concrete under monotonic dynamic loadings, Cem. Concr. Compos. 87 (2018) 149–163, https://doi.org/10.1016/j.cemconcomp.2017.12.012.
[7] A. Santamaría, V. Ortega-López, M. Skaf, J.A. Chica, J.M. Manso, The study of properties and behavior of self compacting concrete containing electric arc furnace slag (eafs) as aggregate, Ain Shams Eng. J. 11 (1) (2020) 231–243, https://doi.org/10.1016/j.asej.2019.10.001.
[8] Z. Ma, J. Shen, C. Wang, H. Wu, Characterization of sustainable mortar containing high-quality recycled manufactured sand crushed from recycled coarse aggregate, Cem. Concr. Compos. 132 (2022) 104629, https://doi.org/10.1016/j.cemconcomp.2022.104629.
[9] C. Wang, J. Xiao, W. Liu, Z. Ma, Unloading and reloading stress strain relationship of recycled aggregate concrete reinforced with steel/polypropylene fibers under uniaxial low-cycle loadings, Cem. Concr. Compos. 131 (2022) 104597, https://doi.org/10.1016/j.cemconcomp.2022.104597.
[10] S. Chinnu, S. Minnu, A. Bahurudeen, R. Senthilkumar, Recycling of industrial and agricultural wastes as alternative coarse aggregates: a step towards cleaner production of concrete, Constr. Build. Mater. 287 (2021) 123056, https://doi.org/10.1016/j.conbuildmat.2021.123056.
[11] C. Wang, J. Xiao, C. Qi, C. Li, Rate sensitivity analysis of structural behaviors of recycled aggregate concrete frame, J. Build. Eng. 45 (2022) 103634, https://doi.org/10.1016/j.jobe.2021.103634.
[12] H. Wu, R. Hu, D. Yang, Z. Ma, Micro-macro characterizations of mortar containing construction waste fines as replacement of cement and sand: a comparative study, Constr. Build. Mater. 383 (2023) 131328, https://doi.org/10.1016/j.conbuildmat.2023.131328.
[13] E. Lal Mohammadi, E. Khaksar Najafi, P. Zanganeh Ranjbar, M. Payan, R. Jamshidi Chenari, B. Fatahi, Recycling industrial alkaline solutions for soil stabilization by low-concentrated fly ash-based alkali cements, Constr. Build. Mater. 393 (2023) 132083, https://doi.org/10.1016/j.conbuildmat.2023.132083.
[14] J.C.R. Khajeh, A.M.A. Payan, A simple review of cemented nonconventional materials: soil composites, Geotech. Geol. Eng. 38 (2020) 1019–1040, https://doi.org/10.1007/s10706-019-01090-x.
[15] A. Sivakrishna, A. Adesina, P. Awoyera, K. Rajesh Kumar, Green concrete: A review of recent developments, Materials Today: Proceedings 27 (2020) 54–58, International Conference on Recent Advances in Materials and Manufacturing 2019. doi:10.1016/j.matpr.2019.08.202.
[16] A. Chatzopoulos, K.K. Sideris, C. Tassos, Production of concretes using slag aggregates: Contribution of increasing the durability and sustainability of constructions, Case Stud. Constr. Mater. 15 (2021) e00711, https://doi.org/10.1016/j.cscm.2021.e00711.
[17] P. Tamayo, J. Pacheco, C. Thomas, J. de Brito, J. Rico, Mechanical and durability properties of concrete with coarse recycled aggregate produced with electric arc furnace slag concrete, Appl. Sci. 10 (1) (2020), https://doi.org/10.3390/app10010216.
[18] V. Revilla-Cuesta, M. Skaf, J. Romera, V. Ortega-López, Elastic stiffness estimation of aggregate–ITZ system of concrete through matrix porosity and volumetric considerations: explanation and exemplifications, Arch. Civ. Mech. Eng. 22 (2022) 59, https://doi.org/10.1007/s43452-022-00382-z.
[19] A. Santamaría, J.M. Romera, I. Marcos, V. Revilla-Cuesta, V. Ortega-López, Shear strength assessment of reinforced concrete components containing eaf steel slag aggregates, J. Build. Eng. 46 (2022) 103730, https://doi.org/10.1016/j.jobe.2021.103730.
[20] I. Sosa, C. Thomas, J. Polanco, J. Setien, J. Sainz-Aja, P. Tamayo, Durability of high-performance self-compacted concrete using electric arc furnace slag aggregate and cupola slag powder, Cem. Concr. Compos. 127 (2022) 104399, https://doi.org/10.1016/j.cemconcomp.2021.104399.485.
[21] C. Pellegrino, V. Gaddo, Mechanical and durability characteristics of concrete containing EAF slag as aggregate, Cem. Concr. Compos. 31 (9) (2009) 663–671, https://doi.org/10.1016/J.CEMCONCOMP.2009.05.006.
[22] A. Santamaría, A. Orbe, M. Losanez, M. Skaf, V. Ortega-López, J.J. Gonzalez, Self-compacting concrete incorporating electric arc-furnace steel making slag as aggregate, Mater. Des. 115 (2017) 179–193, https://doi.org/10.1016/J.MATDES.2016.11.048.
[23] J.T. San-José, I. Vegas, I. Arribas, I. Marcos, The performance of steelmaking slag concretes in the hardened state, Mater. Des. 60 (2014) 612–619, https://doi.org/10.1016/J.MATDES.2014.04.030.
[24] Y.P. Rojas, E.V. López, M.L. Rodriguez, J.D. Pita, Preparation of concrete mixtures with electric arc furnace slag and recycled ground glass, Journal of Physics: Conference Series 935 (2017) 012010. doi:10.1088/ 1742-6596/935/1/012010.
[25] V. Ortega-López, F. Faleschini, C. Pellegrino, V. Revilla-Cuesta, J.M. Manso, Validation of slag-binder fiber-reinforced self-compacting concrete with slag aggregate under field conditions: durability and real strength development, Constr. Build. Mater. 320 (2022) 126280, https://doi.org/10.1016/j.conbuildmat.2021.126280.
[26] A. Santamaría, A. Orbe, J. San José, J. Gonzalez, A study on the durability of structural concrete incorporating electric steelmaking slags, Constr. Build. Mater. 161 (2018) 94–111, https://doi.org/10.1016/j.conbuildmat.2017.11.121.
[27] Y.R. Alharbi, A.A. Abadel, N. Elsayed, O. Mayhoub, M. Kohail, Mechanical properties of eafs concrete after subjected to elevated temperature, Ain Shams Eng. J. 12 (2) (2021) 1305–1311, https://doi.org/10.1016/j.asej.2020.10.003.
[28] S. Kono, F. Kitamura, E. Yuniarsyia, H. Watanabe, T. Mukai, D.J. Mukai, Efforts to develop resilient reinforced concrete building structures in japan, in: Proceedings of the Fourth Conference on Smart Monitoring, Assess. Rehabil. Civ. Struct. (2017) 13–15, https://doi.org/10.1007/978-981-13-3278-4_6.
[29] S. Prasanth, G. Ghosh, Effect of cracked section properties on the resilience based seismic performance evaluation of a building, Structures 34 (2021) 1021–1033, https://doi.org/10.1016/j.istruc.2021.08.035.
[30] W. Zhang, Q. Zheng, A. Ashour, B. Han, Self-healing cement concrete composites for resilient infrastructures: a review, Compos. Part B: Eng. 189 (2020) 107892, https://doi.org/10.1016/j.compositesb.2020.107892.
[31] H. Rooholamini, R. Sedghi, B. Ghobadipour, M. Adresi, Effect of electric arc furnace steel slag on the mechanical and fracture properties of roller-compacted concrete, Constr. Build. Mater. 211 (2019) 88–98, https://doi.org/10.1016/j.conbuildmat.2019.03.223.
[32] A. Garcia-Llona, V. Ortega-López, I. Piñero, A. Santamaría, M. Aguirre, Effects of fiber material in concrete manufactured with electric arc furnace slag: Experimental and numerical study, Constr. Build. Mater. 316 (2022) 125553, https://doi.org/10.1016/j.conbuildmat.2021.125553.
[33] G. Tiberti, F. Germano, A. Mudadu, G.A. Plizzari, An overview of the flexural post-cracking behavior of steel fiber reinforced concrete, Struct. Concr. 19 (3) (2018) 695–718, https://doi.org/10.1002/suco.201700068.
[34] D.-Y. Yoo, Y.-S. Yoon, N. Banthia, Predicting the post-cracking behavior of normal- and high-strength steel-fiber-reinforced concrete beams, Constr. Build. Mater. 93 (2015) 477–485, https://doi.org/10.1016/j.conbuildmat.2015.06.006.
[35] P. Pujadas, A. Blanco, S. Cavalaro, A. de la Fuente, A. Aguado, The need to consider flexural post-cracking creep behavior of macro-synthetic fiber reinforced concrete, Constr. Build. Mater. 149 (2017) 790–800, https://doi.org/10.1016/j.conbuildmat.2017.05.166.
[36] M. Di Prisco, G. Plizzari, L. Vandewalle, Fibre reinforced concrete: new design perspectives, Mater. Struct. Struct. 42 (2009) 1261–1281, https://doi.org/10.1617/s11527-009-9529-4.
[37] J.T. San-José, J. Manso, Fiber-reinforced polymer bars embedded in a resin concrete: Study of both materials and their bond behavior, Polym. Compos. 27 (2006) 315–322, https://doi.org/10.1002/pc.20188.
[38] J.T. San-José, A. Aguado, J.M. Manso, Viscoelastic behavior of a polyester resin concrete reinforced with nonmetallic bars under bending 550 loads, Polym. Compos. 30 (6) (2009) 791–804, https://doi.org/10.1002/pc.20620.

[39] J.A. Fuente-Alonso, V. Ortega-López, M. Skaf, A. Aragon, J.T. San-José, Performance of fiber-reinforced EAF slag concrete for use in pavements, Constr. Build. Mater. 149 (2017) 629–638, doi:10.1016/ J.CONBUILDMAT.2017.05.174.
[40] V. Ortega-López, A. Garcia-Llona, V. Revilla-Cuesta, A. Santamaría, J. San-José, Fiber-reinforcement and its effects on the mechanical properties of high-workability concretes manufactured with slag as aggregate and binder, J. Build. Eng. 43 (March) (2021) 102548, https://doi.org/10.1016/j.jobe.2021.102548.
[41] B. Hansen, M. Barman, New procedure to evaluate the post-crack behavior of fiber-reinforced concrete, Transp. Res. Rec. 2673 (11) (2019) 573–582, https://doi.org/10.1177/0361198119848408.
[42] F. Liu, W. Ding, Y. Qiao, Experimental investigation on the tensile behavior of hybrid steel-pva fiber reinforced concrete containing fly ash and slag powder, Constr. Build. Mater. 241 (2020) 118000, https://doi.org/10.1016/j.conbuildmat.2020.118000.
[43] M.B. Bankir, U. Korkut Sevim, Performance optimization of hybrid fiber concretes against acid and sulfate attack, J. Build. Eng. 32 (2020) 101443, https://doi.org/10.1016/j.jobe.2020.101443.
[44] F. Laranjeira, C. Molins, A. Aguado, Predicting the pullout response of inclined hooked steel fibers, Cem. Concr. Res. 40 (2010) 1471–1487, https://doi.org/10.1016/j.cemconres.2010.05.005.
[45] H. Pakravan, M. Latifi, M. Jamshidi, Hybrid short fiber reinforcement system in concrete: a review, Constr. Build. Mater. 142 (2017) 280–294, https://doi.org/10.1016/j.conbuildmat.2017.03.059.
[46] L.G. Sorelli, A. Meda, G.A. Plizzari, Bending and uniaxial tensile tests on concrete reinforced with hybrid steel fibers, J. Mater. Civ. Eng. 17 (5) (2005) doi: 10.1061/(ASCE)0899-1561(2005)17: 5(519).
[47] K. Wille, S. El-Tawil, A. Naaman, Properties of strain hardening ultra high performance fiber reinforced concrete (UHP-FRC) under direct tensile loading, Cem. Concr. Compos. 48 (2014) 53–66, https://doi.org/10.1016/j.cemconcomp.2013.12.015.
[48] C. Wang, H. Wu, C. Li, Hysteresis and damping properties of steel and polypropylene fiber reinforced recycled aggregate concrete under uniaxial low-cycle loadings, Constr. Build. Mater. 319 (2022) 126191, https://doi.org/10.1016/j.conbuildmat.2021.126191.
[49] D. Shen, X. Shi, S. Zhu, X. Duan, J. Zhang, Relationship between tensile Young's modulus and strength of fly ash high strength concrete at early age, Constr. Build. Mater. 123 (2016) 317–326, https://doi.org/10.1016/J.CONBUILDMAT.2016.06.145.
[50] J. Barros, V. Cunha, A. Ribeiro, J. Antunes, Post-cracking behaviour of steel fiber reinforced concrete, Mater. Struct. 38 (2005) 47–56, https://doi.org/10.1617/14058.
[51] N. Buratti, C. Mazzotti, M. Savoia, Post-cracking behaviour of steel and macro-synthetic fibre-reinforced concretes, Constr. Build. Mater. 25 (5) (2011) 2713–2722, https://doi.org/10.1016/j.conbuildmat.2010.12.022.
[52] M. Soutsos, T. Le, A. Lampropoulos, Flexural performance of fibre reinforced concrete made with steel and synthetic fibres, Constr. Build. Mater. 36 (2012) 704–710, https://doi.org/10.1016/j.conbuildmat.2012.06.042.
[53] V. Revilla-Cuesta, V. Ortega-López, M. Skaf, E. Pasquini, M. Pasetto, Preliminary validation of steel slag-aggregate concrete for rigid pavements: a full-scale study, Infrastructures 6 (5) (2021), https://doi.org/10.3390/infrastructures6050064.
[54] O.L. Manzoli, A.L. Gamino, E.A. Rodrigues, G.K. Claro, Modeling of interfaces in two-dimensional problems using solid finite elements with high aspect ratio, Comput. Struct. 94-95 (2012) 70–82, https://doi.org/10.1016/j.compstruc.2011.12.001.
[55] O.L. Manzoli, M.A. Maedo, L.A. Bitencourt, E.A. Rodrigues, On the use of finite elements with a high aspect ratio for modeling cracks in quasibrittle materials, Eng. Fract. Mech. 153 (2016) 151–170, doi:61010.1016/j.engfracmech.2015.12.026.
[56] E.A. Rodrigues, O.L. Manzoli, L.A. Bitencourt Jr, T.N. Bittencourt, 2D mesoscale model for concrete based on the use of interface element with a high aspect ratio, Int. J. Solids Struct. 94-95 (2016) 112–124, https://doi.org/10.1016/j.ijsolstr.2016.05.004.
[57] J. Segura, I. Carol, Numerical modelling of pressurized fracture evolution in concrete using zero-thickness interface elements, Eng. Fract. Mech. 77 (9) (2010) 1386–1399, https://doi.org/10.1016/j.engfracmech.2010.03.014.
[58] Y. Zhan, G. Meschke, Multilevel computational model for failure analysis of steel-fiber–reinforced concrete structures, J. Eng. Mech. 142 (11) (2016) 04016090, https://doi.org/10.1061/(ASCE)EM.1943-7889.0001154.
[59] Y. Zhan, G. Meschke, Adaptive crack modeling with interface solid elements for plain and fiber reinforced concrete structures, Materials 10 (7) (2017), https://doi.org/10.3390/ma10070771.
[60] M. Pinto, P. Emilio, Method of analysis for cyclically loaded R. C. plane frames including changes in geometry and non-elastic behaviour of elements under combined normal force and bending, in: ABSE Sympoium on Resistance and Ultimate Deformability of Structures Acted on by Well-Defined Repeated Loads, 1973.
[61] M. Barbato, Efficient finite element modelling of reinforced concrete beams retrofitted with fibre reinforced polymers, Comput. Struct. 87 (34) (2009) 167–176, https://doi.org/10.1016/j.compstruc.2008.11.006.
[62] M. Bosco, E. Ferrara, A. Ghersi, E.M. Marino, P.P. Rossi, Improvement of the model proposed by Menegotto and Pinto for steel, Eng. Struct. 124 (2016) 442–456, https://doi.org/10.1016/j.engstruct.2016.06.037.
[63] V. Papadopoulos, J. Murcia-Delso, P. Benson Shing, UC San Diego UC San Diego previously published works title development of headed bars in slab-column joints of reinforced concrete slab bridges publication date, Acids Struct. J. 115 (2018), https://doi.org/10.14359/51702247.
[64] T. Ravi Mullapudi, A. Ayoub, Modeling of the seismic behavior of shear critical reinforced concrete columns, Eng. Struct. 32 (11) (2010) 3601–3615, https://doi.org/10.1016/j.engstruct.2010.08.004.
[65] A. Stavridis, P.B. Shing, Finite-element modeling of nonlinear behavior of masonry-infilled RC frames, J. Struct. Eng. 136 (3) (2010) 285–296, https://doi.org/10.1061/(ASCE)ST.1943-541X.116.
[66] I. Koutromanos, A. Stavridis, P.B. Shing, K. Willam, Numerical modeling of masonry-infilled RC frames subjected to seismic loads, Comput. Struct. 89 (11) (2011) 1026–1037, https://doi.org/10.1016/j.compstruc.2011.01.006.
[67] L. Zongjin, Advanced concrete technology, John Wiley & Sons, Inc, 2011.
[68] A. Santamaría, E. Roji, M. Skaf, I. Marcos, J.J. Gonzalez, The use of steelmaking slags and fly ash in structural mortars, Constr. Build. Mater. 106 (2016) 364–373, https://doi.org/10.1016/J.CONBUILDMAT.2015.12.121.
[69] A. Santamaría, A. Garcia-Llona, V. Revilla-Cuesta, I. Piñero, V. Ortega-López, Bending tests on building beams containing electric arc furnace slag and alternative binders and manufactured with energy-saving placement techniques, Structures 32 (March) (2021) 1921–1933, https://doi.org/10.1016/j.istruc.2021.04.003.
[70] UNE-EN 12390-3, Compressive strength of test specimens (2014).
[71] UNE-EN 12390-13, Determination of secant modulus of elasticity in compression (2014).
[72] UNE-EN 14651+A1, Test method for metallic fibre concrete. Measuring the flexural tensile strength. (2008).
[73] I. Karaman, H. Sehitoglu, Y.I. Chumlyakov, H.J. Maier, I.V. Kireeva, The effect of twinning and slip on the bauschinger effect of hadfield steel single crystals, Metall. Mater. Trans. A: Phys. Metall. Mater. Sci. 32 (13) (2001) 695–706, doi: 665 10.1007/s11661-001-1005-x.
[74] A.P. Parker, E. Troiano, J.H. Underwood, C. Mossey, Characterization of steels using a revised kinematic hardening model incorporating bauschinger effect, J. Press. Vessel Technol. 125 (3) (2003) 277–281, https://doi.org/10.1115/1.1593071.
[75] F. Yoshida, T. Uemori, A model of large-strain cyclic plasticity describing the Bauschinger effect and workhardening stagnation, Int. J. Plast. 18 (5-6) (2002) 661–686, https://doi.org/10.1016/S0749-6419(01)00050-X.
[76] G. Ruiz, M. Elices, J. Planas, Experimental study of fracture of lightly reinforced concrete beams, Mater. Struct. 31 (1998) 683–691, https://doi.org/10.1007/BF02480445.